Gene combinations driving transformation of tubal epithelial organoids and differential sensitivity to high-grade serous ovarian carcinoma drugs

Daryl J. Phuong[1,2], Coulter Q. Ralston[1,3], Tony M. Ezzat[1], Christian S. Ashe[1], Amanda P. Armstrong[1], Andrea Flesken-Nikitin[1], Robert J. Yamulla[1,4], Alexander Yu. Nikitin[1*], John C. Schimenti[1,2*]

[1] Cornell University, College of Veterinary Medicine, Department of Biomedical Sciences, Ithaca, NY 14853, USA

[2] Cornell University, College of Agriculture and Life Sciences, Department of Molecular Biology and Genetics, Ithaca, NY, 14853, USA

[3] Meinig School of Biomedical Engineering, Cornell University, Ithaca, New York, 14853, USA

[4] Illumina, Inc. 5200 Illumina Way, San Diego, CA 92122, USA

* Corresponding authors: A. Nikitin (an58@cornell.edu) and J. Schimenti (jcs92@cornell.edu)

ABSTRACT

High-grade serous ovarian carcinoma (HGSC) is the sixth leading cause of female death from cancer. The majority of HGSC cases are likely to arise from the Fallopian tubal epithelium (TE), while some carcinomas may originate from the ovarian surface epithelium (OSE). Individual tumors bear numerous mutations with uncertain roles in carcinogenesis. To identify mutation combinations that drive transformation and pathological phenotypes, we used a TE-derived organoid platform to screen, *en masse*, 20 candidate HGSC driver genes via combinatorial CRISPR mutagenesis (>7 per clonal organoid). In addition to known drivers (*Brca1*, *Brca2, Nf1, Rb1, Trp53*, and *Pten*), mutations of *Cdkn2a* and *Map2k4* were identified as being critical for TE transformation. *Brca2* and *Map2k4* mutations were not identified in previous OSE screens. Despite both *Map2k4* and *Nf1* being part of the RAS pathway, they led to distinct tumor types: *Map2k4* mutations gave rise to papillary carcinomas that more closely resemble typical HGSC, while *Nf1* mutations resulted in poorly differentiated mesenchymal-like neoplasms. Additionally, different combinations of mutations affected the sensitivity or resistance of transformed organoid cells to drugs commonly used to treat HGSC, with varying responses depending on the presence or absence of the Rho kinase inhibitor, ROCKi. Our findings support the notion that specific HGSC gene disruptions reflect the cell of origin, drive pathological subtypes, and influence differential cancer drug responsiveness.

INTRODUCTION

The transformation of normal cells into cancer cells is driven by multiple genetic events. However, pinpointing the exact combination of mutations that fuel cancer progression and which influence treatment responses is challenging. High-grade serous carcinoma (HGSC) accounts for over 70% of ovarian cancer deaths (1), and TCGA data (available at cBioportal.org) reveal an average of 46 mutations per HGSC sample. Chromosomal rearrangements that disrupt key tumor suppressors like *RB1, NF1, RAD51B*, and *PTEN* have been valuable for identifying key drivers of HGSC (1–8). Furthermore, combinations of somatic and germline mutations play a critical role in determining patient outcomes, tumor characteristics, and immune responses, highlighting why sequencing individual tumors is key to personalized treatment (1,5). Although *TP53* mutations are present in >90% of HGSCs, *Trp53* ablation alone is insufficient for HGSC induction in mice; alterations of 1-3 additional genes are necessary (8–11).

HGSC originates from both ovarian surface epithelium (OSE) and tubal epithelium (TE) cells (7,12–15), but whether they share the same genetic drivers for malignant transformation is unclear. Studies show up to 60% of HGSCs are linked to serous tubal intraepithelial carcinoma (STIC) lesions (16–20), with STICs found in 8% of patients with *BRCA1/2* mutations undergoing risk-reducing salpingo-oophorectomy (18,21–25). Although HGSC was originally believed to only be of OSE origin, mounting evidence suggests that the preponderance of cases arise from the TE (2,20,26).

Arguably, organoids are a more biologically relevant model than traditional 2-D cell cultures for studying cancer biology. Mouse OSE and TE organoids have been used to identify HGSC cell origins and to validate key genetic drivers like *Trp53* and *Rb1* (10,11,27). For example, TE organoids with *Trp53*, *Brca1*, and *Nf1* mutations showed higher tumorigenic potential than OSE organoids with the same mutations (10), supporting the notion that tumors arising from different cell types are driven by distinct mutational landscapes and cell interactions (3,28). The complexity of mutational load in different HGSCs challenges the practical use of predefined gene combinations, especially in genetically

engineered mouse models that acquire secondary mutations similar to those in humans (29). Organoids offer a platform to explore additional genes, mutation combinations, and drug sensitivities in HGSC.

HGSC is classified into four molecular subtypes associated with tumor progression - immunoreactive, proliferative, mesenchymal, and differentiated - though their prognostic value for patient survival remains unclear (30–35). Pathologically, HGSC can present in various patterns the most common of which are papillary, glandular, solid, or SET (solid, pseudoendometrioid, transitional) (31,36,37). *Brca1* mutations are often associated with SET tumors and the immunoreactive subtype (38–40). However, over 70% of HGSC cases are diagnosed at advanced stages, complicating the identification of early genetic drivers and their impact on subtypes and histology (41–43).

To identify genetic drivers of TE transformation, we coupled an organoid platform with random combinatorial mutagenesis. This approach allowed us to induce mutations in seven or more HGSC-associated genes simultaneously. Remarkably, different mutational combinations led to phenotypic variation at the organoid level and resulted in diverse cancer pathologies when transplanted into mice. For example, *Map2k4* mutations drove papillary carcinoma phenotypes that closely resemble the growth patterns of HGSC - a hitherto unreported feature in mouse organoid derived tumor models. Additionally, *Map2k4*-mutated cells were sensitive to paclitaxel but resistant to trametinib, which is surprising given that most studies link *Map2k4* mutations to trametinib sensitivity (44,45). Our findings, which reveal a preferential mesenchymal phenotype associated with *Nf1* mutations and a papillary-glandular phenotype driven by *Map2k4* mutations, underscore the importance of studying specific mutation combinations to unravel the mechanisms of carcinogenesis and to evaluate targeted therapeutic strategies.

RESULTS

Approach for screening candidate HGSC suppressors in a TE organoid model

We leveraged a combinatorial CRISPR/Cas9 mutagenesis screen in TE organoids as a high-throughput platform for identifying mutation combinations that drive HGSC. TE organoids have several important properties for the task: they can form from single cells (Sup. Fig. 1A, B), express key differentiation markers (acetylated alpha-tubulin/FOXJ1 for ciliated cells, OVGP1 for secretory cells, and PAX8 for immature cells) (Sup. Fig. 1C) (10,11,15,46), and if genetically transformed they exhibit morphological changes linked to increased tumorigenic potential in mice (10,11,46). The mutagenesis screen involved infecting individual TE organoid-derived cells (derived from the uterine tube) with a lentiviral library at high multiplicity of infection (MOI), then allowing them to form new organoids. Those with abnormal morphologies were selected, and the gRNAs borne by each were detected (Fig. 1). Prior to screening, the gRNA distribution of the library was determined as a baseline for identification of enriched targeting vectors in aberrant organoid clones (Sup. Fig. 1D, E). We confirmed that secondary organoids were clonal, since cells independently infected with GFP or mCherry reporters, then mixed, formed organoids without dual reporter expression (Sup. Fig. 1B).

Identification of target genes enriched in aberrant organoids

We designed the screen to target 20 genes, 18 of which are commonly mutated in HGSC (based on TCGA data) and two others, *Fancm* and *Apc*, that are also cancer-related (33,47). A lentiviral library consisted of three gRNAs per gene was cloned into a plasmid vector (lentiCRISPRv2) designed to express both the gRNA and Cas9, packaged as lentiviruses, and used to infect TE organoid-forming cells at an estimated multiplicity of infection (MOI) of 7 (Fig. 1). Given that *TP53* mutations are found in over 90% of HGSC cases, the organoids were grown in Nutlin-3a to select for *Trp53*-deficient cells (Fig. 1) (47). After 14 days, we visually screened for abnormal organoids - those with folds, grapelike structures, protrusions, solid formations, or larger sizes compared to controls lacking only *Trp53* (Fig.

2A). The fraction of aberrant organoids was 0.28% ± SD = 0.0311 (n=5 independent library infections). We then picked and expanded these organoids, extracted DNA to sequence vector amplicons, and found that individual organoids had an average of 8 gRNAs (Fig. 2B). Although we expected that all the clones would contain a gRNA targeting *Trp53* due to Nutlin-3A selection, 11 of 95 did not; it is possible that the lentivirus did not stably integrate in these clones (yet they survived short term puromycin selection), or that *Trp53* was poorly expressed or inactivated by other means in these organoids.

After adjusting for vector representation in the plasmid library used to package lentivirus, the most dramatically enriched gRNAs corresponded to *Map2k4* and *Brca1* (Fig. 2C), whereas several were highly underrepresented, notably *Brca2*. The underrepresentation of other vectors may reflect either a compromise to viability or a dependency of co-mutation with certain other genes in order to confer abnormal organoid phenotypes. For example, *Nf1* and *Cdkn2a*, which were not enriched when considering their overall normalized representation (Fig. 2C), were amongst the most statistically enriched in pairwise combinations (Fig. 2D). The most enriched triple mutant combinations (all including *Trp53,* abbreviated "T") involved *Nf1* (N)*, Map2k4* (M), *Cdkn2a* (C)*, Rb1* (R)*, Pten* (P)*, Brca2* (B2) and *Brca1* (B1) and will henceforth be abbreviated as indicated when in combinations (Fig. 2D, E).

Key mutation combinations driving TE transformation

To validate the combinatorial contribution of gene disruptions to transformation, we infected organoid-forming TE cells with specific pairs or trios of lentiviral vectors. Co-mutations of *Nf1* or *Pten* with *Trp53* increased the fraction of aberrant organoids (Fig. 3A, B), consistent with previous findings that loss of *Nf1* and *Pten* drives HGSC (46). *Nf1* mutations resulted in larger organoids with fold structures and intact lumens, while *Pten* mutations caused blob-like protrusions with denser cores (Fig. 3E). In contrast, other double mutations reduced organoid diameter and formation rate (Fig. 3A-D). The TB1 combination, showing poor organoid growth, aligns with previous data suggesting homozygous *Brca1* loss is rare in rapidly growing organoid systems (10).

Trp53 mutations with homozygous *Nf1* and *Pten* deletions are present in 1.26% of human HGSCs (Firehose legacy data in cBioPortal), and TE organoids with these mutations form HGSC-like tumors upon transplantation (46). We generated specific triple mutant organoid combinations to validate the bulk (Fig. 2E) screen results. Disruption of genes besides *Pten* enhanced transformation with TN deficiency, particularly mutations in *Map2k4*, *Cdkn2a*, *Rb1*, or *Brca2*, which increased transformation compared to *Trp53* alone. However, only *Pten* or *Brca2* mutation markedly enhanced transformation in TN-deficient organoids (Fig. 3A, B). The TNB1 combination resulted in poor growth *ex vivo* (10) (Fig. 3C). Our data (Fig. 3A, B) supports previous findings showing that TNP disruption increased aberrant organoid formation rate (46). Interestingly, the phenotype of these organoids was a hybrid of those with TN and TP mutation combinations, exhibiting less overall folding but more ruffled edges and smaller blob-like protrusions (Fig. 3E).

The most overrepresented targeted gene in the screen was *Map2k4*, which acts in the RAS pathway and is considered a potential HGSC tumor suppressor (48,49) but hasn't been functionally studied in mice or organoids for involvement in ovarian cancer. In TCGA data, *MAP2K4* mutations and homozygous deletions are found in 0.32% and 4.2% of HGSC cases, respectively (50). Mutation of the RAS suppressor *Nf1* enhanced TE organoid transformation as described previously (Fig. 3A) in triple mutation combinations compared to double mutants (Fig. 3B, E). *Map2k4* mutations also increased transformation with additional mutations except for *Brca2* but had less impact on organoid diameter than *Nf1* (Fig. 3C, F). Interestingly, TMB1 mutants showed increased transformation, while TMB2 did not - opposite to the patterns seen in TNB1 and TNB2 (Fig. 3A, B). This aligns with the screen's overrepresentation of *Map2k4* and *Brca1* (Fig. 2C).

We next investigated the role of *Cdkn2a*, as it was the third most co-mutated gene in triple mutation combinations with *Trp53* in the screen (Fig. 3E). *Cdkn2a* encodes p14 and p16 proteins, which are involved in the RB pathway and often used to distinguish HGSC from other ovarian cancers (51). Co-mutating *Cdkn2a* with *Trp53* reduced transformation potential, organoid size, and formation rate compared to *Trp53* alone (Fig. 3A-D). Adding *Rb1* to TC only slightly improved these parameters, while

Brca1/2 additions restored them to levels similar to *Trp53* alone. Only *Nf1*, *Map2k4*, or *Pten* co-mutations further improved transformation (Fig. 3A-D). TCP organoids resembled TMP in phenotype (Fig. 3E).

We analyzed HGSC samples with *TP53* mutations and identified the most significant triple mutations as *Map2k4/Cdkn2a* and *Nf1/Pten* (Sup. Fig. 4A, B). For transformed organoids, additional overrepresented mutations included [*Nf1, Pten, Brca2, Crebbp, Rad51, Wwox*] and [*Map2k4, Cdkn2a, Brca1, Lrp1b, Crebbp*] (Sup. Fig. 4A, B). Quadruple mutant combinations TNP*Rad51C* and TMCP enhanced transformation (Sup. Fig. 4C, D). Organoid formation frequency increased with co-mutation of *Map2k4, Cdkn2a, Brca1, Lrp1b*, or *Csmd3* in a TNP deficient background, and *Rb1* or *Csmd3* increased formation with TMC (Sup. Fig. 4C, D). Our findings suggest that while a fourth mutation does not significantly enhance transformation in most cases, it does not rule out roles in cell growth, survival, metastasis, and chemoresistance, warranting further exploration of novel triple combinations.

Mutation combinations influence responses to common HGSC therapeutics

Modern precision cancer treatment has been revolutionized by considering the key genes involved in a person's cancer. When cancer cells survive and gain mutations that promote resistance following first-line treatments, patient survival is often poor. For example, platinum-based therapeutics are initially highly effective but become less successful with each round of treatment (52). Therefore, integrating genetics with treatment modalities is integral for improving patient outcomes. The organoid platform enables facile screening of anticancer agents that are most effective against transformed cells bearing various mutant combinations. To test how TE organoids bearing different genetic combinations respond to common HGSC treatments, we performed dose-response survivability assays with carboplatin (a cisplatin analog causing DNA crosslinks), gemcitabine (a base analog that inhibits DNA replication), niraparib (PARP inhibitor), paclitaxel (a microtubule inhibitor that blocks mitosis), and trametinib (MEK inhibitor), with or without ROCK (Rho-associated protein kinase) inhibitor (ROCKi; a disruptor of cytoskeletal function).

Removing ROCKi from the culture media increased resistance (increased in the inhibitory concentration) of transformed organoids to carboplatin (180%), gemcitabine (122%), and niraparib (133%), while paclitaxel sensitivity remained unchanged and trametinib became more effective (64%) (Sup. Fig. 5A). In the presence of ROCKi, *Nf1*-deficient organoids were 24% more resistant to carboplatin than other combinations (Fig. 4A), likely due to rapid proliferation allowing platinum-resistant organoids to regrow. Without ROCKi, *Rb1/Cdkn2a* mutant organoids showed no change in gemcitabine response, but ROCKi increased resistance of mutants by 28% (Fig. 4B). *Map2k4* mutants were generally more sensitive to paclitaxel (Fig. 4C). Trametinib, a treatment for neurofibromatosis, had a similar impact on cells regardless of *Nf1* status when ROCKi was absent, but ROCKi conferred resistance in *Nf1* mutants (Fig. 4E). Interestingly, TNM cells were unaffected by trametinib, contrary to expectations, as we expected *Map2k4* mutations to act similarly to *Nf1* mutations (Fig. 4E). Removal of ROCKi increased resistance in *Map2k4* mutants, while no correlation between *Map2k4* mutations and trametinib sensitivity was seen with ROCKi (Fig. 4E). There were differences between treatments with and without ROCKi, with some mutations becoming more sensitive while others becoming more resistant (Fig. 4F). These results, particularly the high resistance in TNM combinations, demonstrate the need to study specific mutational perturbations.

Mutation combinations drive differences in tumorigenic potential, gene expression and tumor pathology

To assess whether mutation combinations linked to aberrant organoid formation and morphology reflect *in vivo* tumorigenic potential, we performed subcutaneous flank injections of organoid derived cells into immunodeficient (NSG) female mice and monitored them for up to 200 days. Loss of *Trp53* alone did not result in tumor formation, consistent with prior studies (2,5,7). Among the combinations tested, TNP led to the shortest survival, with tumors reaching 1 cm within an average of 70 days post-injection (Fig. 5A). In contrast, survival times were longer for TN (138 days) and TP (172 days)

combinations (Fig. 5A). Adding *Brca2* (136 days) or *Map2k4* (124 days) to the TN background had minimal impact on survival (Fig. 5A).

In the context of TP deficiency, additional mutations in *Map2k4* or *Cdkn2a* reduced survival by 46 and 28 days, respectively, but tumor size doubling times increased to 62 and 48 days compared to 27 days for TP alone (Fig. 5A). Tumor latency mirrored these findings, with TPM and TPC averaging 96 and 95 days, respectively, compared to 138 days for TP (though this lacked statistical significance due to small sample size; Fig. 5B). Notably, organoids with TM co-mutations and additional losses in *Cdkn2a, Rb1,* or *Brca1* failed to efficiently form tumors within 200 days. Collectively, these results suggest that *Trp53* loss combined with either *Nf1* or *Pten* constitutes a minimal requirement for tumor formation, and additional losses of *Map2k4, Cdkn2a*, or *Brca2* enhance tumor growth and formation rates.

We next assessed whether organoid metrics - formation, transformation, and diameter (Figs. 3E–G) - predicted mouse survival after tumor induction via organoid-derived cell injections. In general, larger organoid diameter and faster transformation rate, but not formation efficiency, correlated with reduced survival (Fig 5A, C-E). Only the TNP mutations had a significantly higher tumor formation rate and growth than TN or TP, leaving open the possibility that certain mutation combinations might impact tumor presentation.

After subcutaneous transplantation, neoplasms arising from genetically altered TE organoids could be stratified into 3 groups (Figure 6., Sup. Table 1). Organoids containing *Nf1* mutations, such as TN*,* commonly resulted in poorly differentiated mesenchymal-like neoplasms (Figure 6A). Such neoplasms were largely composed of tightly arranged spindle cells, contained low to moderate of amount of cytoplasmic KRT8 and nuclear PAX8, and were marked by a medium to high proliferation index according to nuclear Ki67 immunostaining, and a high number of mitotic figures. Organoids with *Map2k4* mutations predominantly formed carcinomas with slit-like spaces forming labyrinthine patterns typical for HGSC (7/16 vs 3/37 for other mutations Fisher's P=0.0078). Cells of such neoplasms consistently expressed KRT8 and PAX8, and they had regionally variable proliferative indices and high-

grade nuclear atypia. Mixed neoplasms contained mesenchymal and glandular-papillary patterns of growth. All neoplasms invited underlying striated muscles and upper levels of dermis at the place of organoid transplantation. Additionally, we noticed that *Nf1* mutation-containing tumors exhibiting spindle cells were derived from organoids with well-defined lumens, while tumors with glandular patterns arose from organoids with more blob-like structures (Fig. 3H). These findings relate specific genetic alterations to distinct features of HGSC.

DISCUSSION

High-grade serous ovarian carcinoma presents as a heterogeneous solid tumor that is genetically unstable with multiple clonal lineages (53,54). These aspects have made treating HGSC especially challenging in stage III-IV HGSC, where 70% of patients relapse within 3 years (55). Early evidence suggests that HGSC does not follow a typical tumor growth trajectory; instead, dissemination occurs as a single rapid wave late in the tumor's evolutionary trajectory (56). Therefore, affect tumor initiation, progress, and presentation will be pivotal for developing diagnostic tools at earlier stages and improving patient outcomes. Our finding that tumors containing *Map2k4* genetic alterations have more differentiated papillary phenotypes typical for HGSC, provides a potentially useful target for intervention. It also opens a possibility for designing more accurate mouse models of HGSC involving inactivation of *Map2k4.*

Whereas HGSC can originate from both OSE and TE cells it is unknown if they utilize the same driver combinations. In our TE organoid screen, we used the same CRISPR KO mini library and infection conditions as we used in a prior screen of OSE (47). The transformation rates were similar: 0.28% for TE and 0.21% for OSE (47). Both OSE and TE transformation involved key HGSC drivers (*Trp53*, *Cdkn2a*, *Rb1*, *Pten*) (Sup. Fig. 7A) (8,9,11,12,15,47), but TE transformation was further enhanced by *Nf1*, *Map2k4*, *Brca2*, and *Brca1* ablation, while OSE transformation was enhanced by *Fancd2*, *Wwox*, *Gabra6*, and *Fat3* mutations (Sup. Fig. 7B). Notably, combinations like *TNP+Fancd2* or *TMC+Wwox* did not increase TE organoid transformation beyond their core triple mutant counterparts (Sup. Fig. 4C, D). Pathway analysis suggests that genes like *Wwox, Gabra6*, and *Fat3* may regulate the MAPK and AKT pathways, while *Fancd2* is involved in DNA repair and interacts with BRCA1/2 (Fig. 7) (57–67). Despite some gene-specific differences, there may be shared altered pathways during malignant transformation. Other studies have compared the transformation potential of OSE and TE cells in organoid models and found differential results with respect to tumorigenic potential (10,11). However, OSE cells are flat cuboidal cells that exist as a single monolayer

surrounding the ovary whereas TE cells exist in a pseudo-stratified structure that requires a 3D space. To this extent, our screening methods to assess transformation potential by adherence-independent growth (OSE) and aberrant morphology (TE) are more suitable approaches for maintaining cells in their native state. In summary, *Fancd2, Wwox, Gabra6,* and *Fat3* appear OSE-specific, while *Nf1, Map2k4, Brca2*, and *Brca1* are TE-specific, though these findings need further validation in direct comparisons.

Of the seven transformation driver genes identified in our screen, *Map2k4* was the most intriguing. Encoding MKK4 in the RAS-MAPK pathway, *Map2k4* phosphorylates JNK or p38 in a context-dependent manner (44,48,68). Evolutionary analyses of human HGSC suggest that aberrant MAPK signaling is associated with an early evolutionary state, marked by fewer subclones, diploid cancers, and better therapy response (69). Further tumor trajectory analysis implicates *MAP2K4* mutations in metastasis, particularly in the dissemination from the ovary to the omentum and ascites (56). While *Map2k4* overexpression can reduce tumor metastasis (70,71), our data show enhanced organoid transformation when co-mutated with *Nf1, Cdkn2a, Rb1, Pten*, or *Brca1*, though not all combinations formed tumors within 200 days (Sup. Table 1). This suggests that aberrant organoid formation may reflect metastatic potential or tumor subtype presentation, rather than just carcinogenesis (71).

Recent research on HGSC treatment has focused on how genetic perturbations influence responses to common therapies (carboplatin, gemcitabine, niraparib, paclitaxel, trametinib). Other studies have shown that differences in cell of origin and chemoresponse exist (10,11). For instance, WT OSE and TE organoids exhibited differential responses to HGSC treatments, highlighting the impact of culture conditions on drug efficacy. One group has shown that genes regulating similar pathways, such as RAS, have differences in response to common therapeutics that are gene context-dependent, such as MYC^{OE}, $KRAS^{OE}$, or $NF1^{-/-}$ (46). We observed that *Rb1/Cdkn2a* mutant cells responded similarly to gemcitabine regardless of ROCKi addition, though there were two subgroups: one more sensitive in the presence of ROCKi, the other less so. Generally, *Pten* and *Map2k4* mutations increased sensitivity, while *Nf1* mutations contributed to resistance in the presence of ROCKi. Previous

studies have shown that overexpression of *Ccne1* enhances gemcitabine sensitivity (46), and we found *Trp53/Rb1* mutants to be among the most resistant, with *Nf1* mutations maintaining resistance and *Map2k4* mutations increasing sensitivity.

We found that in general there was no difference between paclitaxel treated samples with ROCKi or not. We made the novel finding that *Map2k4* mutants were particularly sensitive to paclitaxel treatment, providing a potentially new avenue of treatment when considering RAS pathway altered cancers, primarily those implicating *Map2k4* and its downstream targets. Other groups have also shown that *Pten* mutations tend to drive resistances when compared to *Nf1* (46), but we found the opposite in our system. Altogether this may be due to differences in culture conditions or assay design. Nonetheless this implores the need to consider the whole tumor and identifying dominant mutations that are important for diagnosis and treatment of patients.

ROCKi (e.g., Fasudil) is emerging as a promising tool in combination therapy due to its roles in cytoskeletal regulation, cell migration, proliferation, survival, and metastasis (72,73). Previous studies have shown its potential to enhance chemo-sensitivity in resistant cancers, such as pancreatic cancer when combined with gemcitabine (74). Our data support this, showing that ROCKi treatment with gemcitabine significantly reduced transformed organoid survival compared to untreated controls (Sup. Fig. 6A). ROCKi also increased sensitivity to carboplatin and niraparib but conferred resistance to trametinib (Sup. Fig. 6A). Notably, transformed TE cells with *Nf1* mutations showed more resistance to paclitaxel than those with *Map2k4* mutations, with no significant difference between ROCKi -treated and untreated conditions. However, *Map2k4* mutations were more resistant to trametinib without ROCKi. These findings suggest that ROCKi could enhance treatment efficacy for specific mutations, offering new therapeutic possibilities.

Here, we present a comprehensive study demonstrating the tumorigenic potential of transformed TE organoids, confirming their utility as a model for studying tumor growth. While previous groups have shown that *TNP* mutations readily form tumors (46), our study goes further by detailing the specific impact of these mutations on tumor progression (Fig. 5). We also show that organoid metrics of

transformation and diameter correlate with patient survival, a previously unreported correlation. Additionally, we report that *Nf1* mutations preferentially form mesenchymal tumors while *Map2k4* mutations preferentially form papillary tumors (Fig. 6). This observation suggest the need to develop new mouse models focused on *Map2k4* mutations.

HGSC is characterized by numerous mutations, which makes identifying driver genes challenging. Our studies highlight the potential of rapidly screening genetic manipulations to explore the cell of origin and genetic drivers in HGSC. For example, our previous OSE screen showed that stem cells are more prone to transformation than non-stem cells (47). Recently we described TE cell lineage hierarchy and reported that inactivation of *Trp53* and *Rb1* in pre-ciliated cells leads to HGSC formation in the mouse (15). Future organoid studies should facilitate pinpointing cells most vulnerable to cancer cell states and their genetic drivers. Our KO screen also confirmed *Map2k4* as a key driver of TE cell transformation, revealing its sensitivity to paclitaxel and resistance to trametinib. Additionally, our platform is amenable to modeling of amplification/overexpression events using CRISPRa (75) and assessing how gene combinations respond to therapies. The high throughput and speed of our platform allowed us to identify novel genetic drivers and optimal treatment strategies and can be further translated into human models to quickly assess patients for the most beneficial treatment outcomes.

METHODS

Experimental animals. NOD.Cg-*Prkdc*^{scid} *Il2rg*$^{tm1wjl/}$SzJ (NSG) mice (Stock number 005557 were obtained from The Jackson Laboratory (Bar Harbor, ME, USA). The number of animals used in every experiment is indicated as biological replicates in Fig. legends and supplementary tables. Animals were euthanized if they became moribund or developed tumors over 1 cm in diameter. All the experiments and maintenance of the mice were conducted under protocols approved by the Cornell University Institutional Laboratory Animal Use and Care Committee (protocols numbers 2000-0116, 2001-0072 and 2004-0038). Mice were housed within a 10/14 light cycle. The lights came on at 5 a.m. and went off at 7 p.m., the humidity ranged from 30 – 70 %, and the ambient temperature was kept at 72°F +/- 2°F.

TE organoid derivation and culture. TE Organoids were cultured and derived as previously described (15). TE cells were isolated and cultured into organoids from 2-3 month old *Gt(ROSA)26Sor*$^{tm9(CAG-tdTomato)Hze}$ (*Rosa-loxp-stop-loxp*-tdTomato/Ai9, Stock number 007909 Jackson Laboratory) were sacrificed, oviducts isolated and dispersed into single cells with collagenase/dispase. Cells were rescued with 20% FBS containing media and plated as rims with matrigel (Corning #356231) at a density of 10kcells/100uL of matrigel per well in a 24w plate. Organoids were then expanded and cultured for at least 5 passages before experiments were performed. Organoids were passaged on day 7 unless otherwise specified. To passage organoids, media was aspirated from the wells, 300uL of cultrex organoid harvesting solution (R&D 3700-100-01) was added to each well and vigorously pipeted to disrupt matrigel. Dissolved matrigel was then transferred to a 15mL conical and allowed to rest on ice for 1hour. Organoids were then spun down at 600xg for 5 minutes at 4C. If matrigel is still present, more cultrex organoid harvesting media was added and incubated for 30 minutes followed by centrifugation as described above. Once all matrigel is gone, supernatant was removed and 1mL of Trypsin EDTA 0.25% (Gibco 25200072) was added and incubated at 37C. Every 5 minutes organoids were disrupted into single cells with a P1000 pipet (vigorous pipetting at least 50 times up and down).

This step was repeated 3 times for a total of 15 minutes. 20% FBS containing media was then added and cells were pelleted as described above. Cells were then resuspended in TE media and counted to be passaged as described above.

Lentiviral production and transduction. Lentivirus were produced in 293T cells and titer determined via limiting dilutions of virus in TE organoid cells as previously described (47). Briefly, 293T cells were seeded into 10cm dishes before LentiCRISPRv2 (Addgene #52961), PMD.2G (Addgene #12259) and PSPAX2 (Addgene #12260) were transfected using Transit-LT1 transfection reagent (Mirus bio, MIR2306) via manufacturer instructions. Virus was collected at 48 and 72 hours post transfection. Lenti-X Concentrator (Takara, 631231) was used as instructed to concentrate virus. Virus was then resuspended in TE organoid media with polybrene (Sigma, TR-1003-G) and frozen at -80C until use. LentiCRISPRv2-GFP (Addgene #82416) reporter plasmid was used to evaluate the quality of virus produced. To titer the virus, 5K TE organoid cells were subjected to limiting dilutions of virus in a 96 well plate and spinoculated at 600xg for 1hour at 37C as previously described (46). Lentiviral transduction continued for 6 hours at 37C in a cell incubator before cells were collected, mixed with matrigel and plated. After 48 hours 2ug/mL of puromycin was used to select for properly infected cells. Infection percent was evaluated by determining the number of surviving cells in treated versus non treated samples. The multiplicity of infection was calculated by using a survival percent below 30% to exclude double infection events. These values were then multiplied and averaged to determine an MOI of 7 (47).

Screen and validation. Day 7 TE organoids were broken into single cell suspensions as described above and infected with the minilibrary at an MOI of 7 and plated at a density of 5K cells per 25uL Matrigel droplet. 48 hours post infection, cells were treated with puromycin (2ug/mL, Sigma, A1113803) and at 96 hours media was changed to contain 10uM Nutlin-3A (SelleckChem, S8059). Media was changed every 2-3 days containing 10uM Nutlin-3A until day 14 where organoid transformation was

assessed. Mutant organoids were then released from Matrigel with a P1000 wide bore tip in cultrex organoid harvesting media and allowed to settle by gravity. Supernatent was aspirated and replaced with more cultrex organoid harvesting media and allowed to settle by gravity. Organoids were then released onto a poly-hema (Sigma, P3932) coated tissue culture plate, picked as whole organoids, expanded in 2D culture, genomic DNA harvested with GeneJET Genomic DNA Purification Kit (Thermo Fisher, K0722), and PCR amplification with the following primers: CTTGGCTTTATATATCTTGTGGAAAGG and CGACTCGGTGCCACTTT was performed with Illumina overhangs also added to each primer. Indexing reactions were performed to barcode each individual colony and pooled. 300bp paired end sequencing was performed using Illumina Miseq to detect gRNA presence in a particular clone at a read depth of 4 million. Each sequenced clone was aligned with a custom built library containing each of the gRNA's in the screen to identify "hits," where genome integration had taken place as described previously (47,75).

After identification of key combinations that result in TE organoid transformation, targeted lentiviral libraries were prepared and single cell suspensions from TE organoids were infected with the libraries at a minimum MOI of 7. Cells were then plated, treated with both puromycin and Nutlin-3A as described above. Organoid transformation rate was determined by counting the total number of aberrant organoids and dividing that by the total number of organoids formed after 14 days of culture. Images were acquired on a Zeiss Axiovert microscope.

Organoid preparation for histological evaluation. Organoids were released with organoid harvesting solution as described above. Organoids were placed on ice for 1 hour to release and allowed to settle to the tube bottom before aspirating the media without disturbing the pellet. Organoids were then washed with 10mL of ice cold 1X PBS to remove any residual Matrigel. Organoids were allowed to settle by gravity, the PBS was aspirated, then fixed in 4% PFA (diluted in PBS) on ice for 1 hour. Organoids were then washed twice with ice cold 1X PBS, then mixed with an equal volume of HistoGel (Epredia, HG4000012) preheated to 65°C and dispensed into dome-shaped molds for embedding.

HistoGel molds set for 10 minutes prior to standard tissue processing, paraffin embedding, and preparation of 4-μm-thick tissue sections followed by immunohistochemistry (15,76).

Mouse tumorigenic studies. According to previous results (10), frequency of tumor formation by mutant TE organoids was not impacted by site (s.c. vs, orthotopic) of organoid transplantation. Targeted library preparation and TE organoid infections were performed as described above. After passaging to expand cells, day 14 organoids were then disrupted into single cells and $5x10^5$ cells were mixed with 100uL of 1X PBS (Gibco 10010023) and Matrigel (Corning #356231) at a 1:1 ratio and injected subcutaneously in the flanks of NSG mice. All mice received bilateral injections and were monitored weekly for tumor formation, and growth of tumors. Mice were sacrificed when tumors reached 1 cm in diameter.

Drug Assays. Organoids were grown and dispersed into single cells as described above. Cells were diluted to a concentration of 100 cells per uL of Matrigel. 10uL of Matrigel containing cells were then seeded per well into the bottom of a black walled clear bottom 96 well plate (Corning #3603) and 100uL of media was added. 1 day after plating, cells were treated with the concentrations of drugs, media was changed on day 3 and on day 5 media was removed and 100uL of 3D Cell titer glo (Promega # G9683) was added for 1hr at room temperature and read on a biotek plate reader (10). Prism 10 was used to fit graphs and interpret IC50 values with the “[inhibitor] vs. response- variable slope (normalized)” option.

Immunohistochemistry and image analysis. For paraffin embedding, organoids and tissues were fixed in 4% paraformaldehyde overnight at 4°C followed by standard tissue processing, paraffin embedding and preparation of 4 μm-thick tissue sections. For immunohistochemistry, antigen retrieval was performed by incubation of deparaffinized and rehydrated tissue sections in boiling 10 mM sodium citrate buffer (pH 6.0) for 10 minutes. The primary antibodies were incubated either at 4°C for overnight

or at room temperature for 2 hours, followed by incubation with secondary biotinylated antibodies (dilution 1:200, 45 minutes, at room temperature, RT). Modified Elite avidin-biotin peroxidase (ABC) technique (Vector Laboratories, Burlingame, CA, USA; pk-6100) was performed at room temperature for 30 minutes. Hematoxylin was used as the counterstain. All primary and secondary antibodies used for immunostaining are listed in Supplementary Table 2. For quantitative studies, sections were scanned by ScanScope CS2 or FL (Leica Biosystems, Vista, CA) with a 40× objective, followed by the analysis with the ImageJ software (National Institutes of Health, Bethesda, MD, USA).

Statistical analyses

Statistical comparisons were performed using a two-tailed Fisher's exact test with InStat 3 and Prism 6 software (GraphPad Software Inc., La Jolla, CA, USA). Prism 10 software was used to perform one-way anova, IC50 calculations, welch's two tailed t-test. Cbioportal was used to perform analysis of human data. χ^2 analysis was performed in excel.

References

1. Patch A-M, Christie EL, Etemadmoghadam D, Garsed DW, George J, Fereday S, et al. Whole-genome characterization of chemoresistant ovarian cancer. Nature. 2015 May 28;521(7553):489–94.

2. Labidi-Galy SI, Papp E, Hallberg D, Niknafs N, Adleff V, Noe M, et al. High grade serous ovarian carcinomas originate in the fallopian tube. Nat Commun. 2017 Oct 23;8(1):1093.

3. Polak P, Karlić R, Koren A, Thurman R, Sandstrom R, Lawrence M, et al. Cell-of-origin chromatin organization shapes the mutational landscape of cancer. Nature. 2015 Feb 19;518(7539):360–4.

4. Sinkala M. Mutational landscape of cancer-driver genes across human cancers. Sci Rep. 2023 Aug 7;13(1):12742.

5. Garsed DW, Pandey A, Fereday S, Kennedy CJ, Takahashi K, Alsop K, et al. The genomic and immune landscape of long-term survivors of high-grade serous ovarian cancer. Nat Genet. 2022 Dec 1;54(12):1853–64.

6. Yang SYC, Lheureux S, Karakasis K, Burnier JV, Bruce JP, Clouthier DL, et al. Landscape of genomic alterations in high-grade serous ovarian cancer from exceptional long- and short-term survivors. Genome Med. 2018 Oct 31;10(1):81.

7. Zhai Y, Wu R, Kuick R, Sessine MS, Schulman S, Green M, et al. High-grade serous carcinomas arise in the mouse oviduct via defects linked to the human disease. J Pathol. 2017 Sep;243(1):16–25.

8. Flesken-Nikitin A, Hwang C-I, Cheng C-Y, Michurina TV, Enikolopov G, Nikitin AY. Ovarian surface epithelium at the junction area contains a cancer-prone stem cell niche. Nature. 2013 Mar 14;495(7440):241–5.

9. Flesken-Nikitin A, Choi K-C, Eng JP, Shmidt EN, Nikitin AY. Induction of carcinogenesis by concurrent inactivation of p53 and Rb1 in the mouse ovarian surface epithelium. Cancer Res. 2003 Jul 1;63(13):3459–63.

10. Lõhmussaar K, Kopper O, Korving J, Begthel H, Vreuls CPH, van Es JH, et al. Assessing the origin of high-grade serous ovarian cancer using CRISPR-modification of mouse organoids. Nat Commun. 2020 May 27;11(1):2660.

11. Zhang S, Dolgalev I, Zhang T, Ran H, Levine DA, Neel BG. Both fallopian tube and ovarian surface epithelium are cells-of-origin for high-grade serous ovarian carcinoma. Nat Commun. 2019 Nov 26;10(1):5367.

12. Perets R, Wyant GA, Muto KW, Bijron JG, Poole BB, Chin KT, et al. Transformation of the fallopian tube secretory epithelium leads to high-grade serous ovarian cancer in Brca;Tp53;Pten models. Cancer Cell. 2013 Dec 9;24(6):751–65.

13. Kim J, Coffey DM, Creighton CJ, Yu Z, Hawkins SM, Matzuk MM. High-grade serous ovarian cancer arises from fallopian tube in a mouse model. Proc Natl Acad Sci USA. 2012 Mar 6;109(10):3921–6.

14. Maniati E, Berlato C, Gopinathan G, Heath O, Kotantaki P, Lakhani A, et al. Mouse ovarian cancer models recapitulate the human tumor microenvironment and patient response to treatment. Cell Rep. 2020 Jan 14;30(2):525-540.e7.

15. Flesken-Nikitin A, Ralston CQ, Fu D-J, De Micheli AJ, Phuong DJ, Harlan BA, et al. Pre-ciliated tubal epithelial cells are prone to initiation of high-grade serous ovarian carcinoma. Nat Commun. 2024 Oct 5;15(1):8641.

16. Chong GO, Park JY, Lee HJ. Incidental Serous Tubal Intraepithelial Carcinoma that Developed into Primary Peritoneal Serous Carcinoma in a Patient without BRCA Mutation. Am J Case Rep. 2020 Feb 8;21:e921146.

17. Patrono MG, Iniesta MD, Malpica A, Lu KH, Fernandez RO, Salvo G, et al. Clinical outcomes in patients with isolated serous tubal intraepithelial carcinoma (STIC): A comprehensive review. Gynecol Oncol. 2015 Dec;139(3):568–72.

18. Saccardi C, Zovato S, Spagnol G, Bonaldo G, Marchetti M, Alessandrini L, et al. Efficacy of risk-reducing salpingo-oophorectomy in BRCA1-2 variants and clinical outcomes of follow-up in patients with isolated serous tubal intraepithelial carcinoma (STIC). Gynecol Oncol. 2021 Nov;163(2):364–70.

19. Weinberger V, Bednarikova M, Cibula D, Zikan M. Serous tubal intraepithelial carcinoma (STIC) - clinical impact and management. Expert Rev Anticancer Ther. 2016 Dec;16(12):1311–21.

20. Ducie J, Dao F, Considine M, Olvera N, Shaw PA, Kurman RJ, et al. Molecular analysis of high-grade serous ovarian carcinoma with and without associated serous tubal intra-epithelial carcinoma. Nat Commun. 2017 Oct 17;8(1):990.

21. Powell CB, Swisher EM, Cass I, McLennan J, Norquist B, Garcia RL, et al. Long term follow up of BRCA1 and BRCA2 mutation carriers with unsuspected neoplasia identified at risk reducing salpingo-oophorectomy. Gynecol Oncol. 2013 May;129(2):364–71.

22. Kauff ND, Satagopan JM, Robson ME, Scheuer L, Hensley M, Hudis CA, et al. Risk-reducing salpingo-oophorectomy in women with a BRCA1 or BRCA2 mutation. N Engl J Med. 2002 May 23;346(21):1609–15.

23. Rhiem K, Foth D, Wappenschmidt B, Gevensleben H, Büttner R, Ulrich U, et al. Risk-reducing salpingo-oophorectomy in BRCA1 and BRCA2 mutation carriers. Arch Gynecol Obstet. 2011 Mar;283(3):623–7.

24. Smith MJ, Gerber D, Olsen A, Khouri OR, Wang Y, Liu M, et al. Uptake and timing of risk-reducing salpingo-oophorectomy among patients with BRCA1 and BRCA2 mutations. Am J Obstet Gynecol. 2021 Nov;225(5):508.e1-508.e10.

25. Kauff ND, Barakat RR. Risk-reducing salpingo-oophorectomy in patients with germline mutations in BRCA1 or BRCA2. J Clin Oncol. 2007 Jul 10;25(20):2921–7.

26. Shih I-M, Wang Y, Wang T-L. The origin of ovarian cancer species and precancerous landscape. Am J Pathol. 2021 Jan;191(1):26–39.

27. Kopper O, de Witte CJ, Lõhmussaar K, Valle-Inclan JE, Hami N, Kester L, et al. An organoid platform for ovarian cancer captures intra- and interpatient heterogeneity. Nat Med. 2019 May;25(5):838–49.

28. Fiorini E, Veghini L, Corbo V. Modeling cell communication in cancer with organoids: making the complex simple. Front Cell Dev Biol. 2020 Mar 18;8:166.

29. McCool KW, Freeman ZT, Zhai Y, Wu R, Hu K, Liu C-J, et al. Murine Oviductal High-Grade Serous Carcinomas Mirror the Genomic Alterations, Gene Expression Profiles, and Immune Microenvironment of Their Human Counterparts. Cancer Res. 2020 Feb 15;80(4):877–89.

30. Khashaba M, Fawzy M, Abdel-Aziz A, Eladawei G, Nagib R. Subtyping of high grade serous ovarian carcinoma: histopathological and immunohistochemical approach. J Egypt Natl Canc Inst. 2022 Feb 9;34(1):6.

31. Murakami R, Matsumura N, Mandai M, Yoshihara K, Tanabe H, Nakai H, et al. Establishment of a Novel Histopathological Classification of High-Grade Serous Ovarian Carcinoma Correlated with Prognostically Distinct Gene Expression Subtypes. Am J Pathol. 2016 May;186(5):1103–13.

32. Chen GM, Kannan L, Geistlinger L, Kofia V, Safikhani Z, Gendoo DMA, et al. Consensus on Molecular Subtypes of High-Grade Serous Ovarian Carcinoma. Clin Cancer Res. 2018 Oct 15;24(20):5037–47.

33. Cancer Genome Atlas Research Network. Integrated genomic analyses of ovarian carcinoma. Nature. 2011 Jun 29;474(7353):609–15.

34. Chen J, Shi X, Xiao L, Li Z, Li Z, Sun L. Better or worse? The prognostic role of the mesenchymal subtype in patients with high-grade serous ovarian carcinoma: A systematic review and meta-analysis. Cancer Med. 2022 Oct;11(20):3761–70.

35. Hu Y, Taylor-Harding B, Raz Y, Haro M, Recouvreux MS, Taylan E, et al. Are epithelial ovarian cancers of the mesenchymal subtype actually intraperitoneal metastases to the ovary? Front Cell Dev Biol. 2020 Jul 17;8:647.

36. Hatano Y, Tamada M, Asano N, Hayasaki Y, Tomita H, Morishige K-I, et al. High-grade serous ovarian carcinoma with mucinous differentiation: report of a rare and unique case suggesting transition from the “SET” feature of high-grade serous carcinoma to the “STEM” feature. Diagn Pathol. 2019 Jan 12;14(1):4.

37. Uner H, Demir M, Goksuluk D, Kars A, Uner M, Usubutun A. Evidence for Diverse Prognosis in High-Grade Serous Ovarian Carcinoma: Solid, Pseudoendometrioid, and Transitional-Like; So-Called “SET Morphology” and Progesterone Receptor Status. Turk Patoloji Derg. 2022;38(3):240–50.

38. Press JZ, De Luca A, Boyd N, Young S, Troussard A, Ridge Y, et al. Ovarian carcinomas with genetic and epigenetic BRCA1 loss have distinct molecular abnormalities. BMC Cancer. 2008 Jan 22;8:17.

39. Zheng M, Hu Y, Gou R, Liu O, Nie X, Li X, et al. Identification of immune-enhanced molecular subtype associated with BRCA1 mutations, immune checkpoints and clinical outcome in ovarian carcinoma. J Cell Mol Med. 2020 Mar;24(5):2819–31.

40. Wei Y, Ou T, Lu Y, Wu G, Long Y, Pan X, et al. Classification of ovarian cancer associated with BRCA1 mutations, immune checkpoints, and tumor microenvironment based on immunogenomic profiling. PeerJ. 2020 Nov 24;8:e10414.

41. González-Martín A, Pothuri B, Vergote I, DePont Christensen R, Graybill W, Mirza MR, et al. Niraparib in Patients with Newly Diagnosed Advanced Ovarian Cancer. N Engl J Med. 2019 Dec 19;381(25):2391–402.

42. Ditzel HM, Strickland KC, Meserve EE, Stover E, Konstantinopoulos PA, Matulonis UA, et al. Assessment of a Chemotherapy Response Score (CRS) System for Tubo-Ovarian High-Grade Serous Carcinoma (HGSC). Int J Gynecol Pathol. 2019 May;38(3):230–40.

43. Moore K, Colombo N, Scambia G, Kim B-G, Oaknin A, Friedlander M, et al. Maintenance Olaparib in Patients with Newly Diagnosed Advanced Ovarian Cancer. N Engl J Med. 2018 Dec 27;379(26):2495–505.

44. Xue Z, Vis DJ, Bruna A, Sustic T, van Wageningen S, Batra AS, et al. MAP3K1 and MAP2K4 mutations are associated with sensitivity to MEK inhibitors in multiple cancer models. Cell Res. 2018 Jul;28(7):719–29.

45. Jansen RA, Mainardi S, Dias MH, Bosma A, van Dijk E, Selig R, et al. Small-molecule inhibition of MAP2K4 is synergistic with RAS inhibitors in KRAS-mutant cancers. Proc Natl Acad Sci USA. 2024 Feb 27;121(9):e2319492121.

46. Zhang S, Iyer S, Ran H, Dolgalev I, Gu S, Wei W, et al. Genetically defined, syngeneic organoid platform for developing combination therapies for ovarian cancer. Cancer Discov. 2021 Feb;11(2):362–83.

47. Yamulla RJ, Nalubola S, Flesken-Nikitin A, Nikitin AY, Schimenti JC. Most Commonly Mutated Genes in High-Grade Serous Ovarian Carcinoma Are Nonessential for Ovarian Surface Epithelial Stem Cell Transformation. Cell Rep. 2020 Sep 1;32(9):108086.

48. Davis SJ, Choong DYH, Ramakrishna M, Ryland GL, Campbell IG, Gorringe KL. Analysis of the mitogen-activated protein kinase kinase 4 (MAP2K4) tumor suppressor gene in ovarian cancer. BMC Cancer. 2011 May 17;11:173.

49. Yang H, Mao W, Rodriguez-Aguayo C, Mangala LS, Bartholomeusz G, Iles LR, et al. Paclitaxel Sensitivity of Ovarian Cancer Can be Enhanced by Knocking Down Pairs of Kinases that Regulate MAP4 Phosphorylation and Microtubule Stability. Clin Cancer Res. 2018 Oct 15;24(20):5072–84.

50. Phuong DJ, Pirtz MG, Ralston CQ, Cosgrove BD, Schimenti JC, Flesken-Nikitin A, et al. Aggressive Serous Carcinomas of the Female Reproductive Tract: Cancer-Prone Cell States and Genetic Drivers. Cancers (Basel). 2025 Feb 11;17(4):604.

51. Sallum LF, Andrade L, Ramalho S, Ferracini AC, de Andrade Natal R, Brito ABC, et al. WT1, p53 and p16 expression in the diagnosis of low- and high-grade serous ovarian carcinomas and their relation to prognosis. Oncotarget. 2018 Mar 23;9(22):15818–27.

52. Uno K, Yoshikawa N, Tazaki A, Ohnuma S, Kitami K, Iyoshi S, et al. Significance of platinum distribution to predict platinum resistance in ovarian cancer after platinum treatment in neoadjuvant chemotherapy. Sci Rep. 2022 Mar 16;12(1):4513.

53. Geistlinger L, Oh S, Ramos M, Schiffer L, LaRue RS, Henzler CM, et al. Multiomic Analysis of Subtype Evolution and Heterogeneity in High-Grade Serous Ovarian Carcinoma. Cancer Res. 2020 Oct 15;80(20):4335–45.

54. Denisenko E, de Kock L, Tan A, Beasley AB, Beilin M, Jones ME, et al. Spatial transcriptomics reveals discrete tumour microenvironments and autocrine loops within ovarian cancer subclones. Nat Commun. 2024 Apr 3;15(1):2860.

55. González-Martín A, Harter P, Leary A, Lorusso D, Miller RE, Pothuri B, et al. Newly diagnosed and relapsed epithelial ovarian cancer: ESMO Clinical Practice Guideline for diagnosis, treatment and follow-up. Ann Oncol. 2023 Oct;34(10):833–48.

56. Sveen A, Johannessen B, Klokkerud SMK, Kraggerud SM, Meza-Zepeda LA, Bjørnslett M, et al. Evolutionary mode and timing of dissemination of high-grade serous carcinomas. JCI Insight. 2024 Feb 8;

57. Liu S, Huang J, Zhang Y, Liu Y, Zuo S, Li R. MAP2K4 interacts with Vimentin to activate the PI3K/AKT pathway and promotes breast cancer pathogenesis. Aging (Albany NY). 2019 Nov 25;11(22):10697–710.

58. Liu C-C, Ho P-C, Lee I-T, Chen Y-A, Chu C-H, Teng C-C, et al. WWOX phosphorylation, signaling, and role in neurodegeneration. Front Neurosci. 2018 Aug 15;12:563.

59. Lo J-Y, Chou Y-T, Lai F-J, Hsu L-J. Regulation of cell signaling and apoptosis by tumor suppressor WWOX. Exp Biol Med (Maywood). 2015 Mar;240(3):383–91.

60. Pavese JM, Ogden IM, Voll EA, Huang X, Xu L, Jovanovic B, et al. Mitogen-activated protein kinase kinase 4 (MAP2K4) promotes human prostate cancer metastasis. PLoS ONE. 2014 Jul 14;9(7):e102289.

61. Baroja I, Kyriakidis NC, Halder G, Moya IM. Expected and unexpected effects after systemic inhibition of Hippo transcriptional output in cancer. Nat Commun. 2024 Mar 27;15(1):2700.

62. Seo S, Kim YA, Lee J, Lee S, Kim J, Lee S. Fat3 regulates neural progenitor cells by promoting Yap activity during spinal cord development. Sci Rep. 2022 Aug 30;12(1):14726.

63. Guo Z, Yan X, Song C, Wang Q, Wang Y, Liu X-P, et al. FAT3 mutation is associated with tumor mutation burden and poor prognosis in esophageal cancer. Front Oncol. 2021 Mar 19;11:603660.

64. Gumireddy K, Li A, Kossenkov AV, Sakurai M, Yan J, Li Y, et al. The mRNA-edited form of GABRA3 suppresses GABRA3-mediated Akt activation and breast cancer metastasis. Nat Commun. 2016 Feb 12;7:10715.

65. Li T-J, Jiang J, Tang Y-L, Liang X-H. Insights into the leveraging of GABAergic signaling in cancer therapy. Cancer Med. 2023 Jul;12(13):14498–510.

66. Bell-Horner CL, Dohi A, Nguyen Q, Dillon GH, Singh M. ERK/MAPK pathway regulates GABAA receptors. J Neurobiol. 2006 Nov;66(13):1467–74.

67. Han B, Shen Y, Zhang P, Jayabal P, Che R, Zhang J, et al. Overlooked FANCD2 variant encodes a promising, portent tumor suppressor, and alternative polyadenylation contributes to its expression. Oncotarget. 2017 Apr 4;8(14):22490–500.

68. Canovas B, Nebreda AR. Diversity and versatility of p38 kinase signalling in health and disease. Nat Rev Mol Cell Biol. 2021 May;22(5):346–66.

69. Lahtinen A, Lavikka K, Virtanen A, Li Y, Jamalzadeh S, Skorda A, et al. Evolutionary states and trajectories characterized by distinct pathways stratify patients with ovarian high grade serous carcinoma. Cancer Cell. 2023 Jun 12;41(6):1103-1117.e12.

70. Spillman MA, Lacy J, Murphy SK, Whitaker RS, Grace L, Teaberry V, et al. Regulation of the metastasis suppressor gene MKK4 in ovarian cancer. Gynecol Oncol. 2007 May;105(2):312–20.

71. Yamada SD, Hickson JA, Hrobowski Y, Vander Griend DJ, Benson D, Montag A, et al. Mitogen-activated protein kinase kinase 4 (MKK4) acts as a metastasis suppressor gene in human ovarian carcinoma. Cancer Res. 2002 Nov 15;62(22):6717–23.

72. McLeod R, Kumar R, Papadatos-Pastos D, Mateo J, Brown JS, Garces AHI, et al. First-in-Human Study of AT13148, a Dual ROCK-AKT Inhibitor in Patients with Solid Tumors. Clin Cancer Res. 2020 Sep 15;26(18):4777–84.

73. Barcelo J, Samain R, Sanz-Moreno V. Preclinical to clinical utility of ROCK inhibitors in cancer. Trends Cancer. 2023 Mar;9(3):250–63.

74. Kim S, Kim SA, Han J, Kim I-S. Rho-Kinase as a Target for Cancer Therapy and Its Immunotherapeutic Potential. Int J Mol Sci. 2021 Nov 29;22(23).

75. Gilbert LA, Horlbeck MA, Adamson B, Villalta JE, Chen Y, Whitehead EH, et al. Genome-scale CRISPR-mediated control of gene repression and activation. Cell. 2014 Oct 23;159(3):647–61.

76. Flesken-Nikitin A, Harlan BA, Nikitin AY. Transplantation into the mouse ovarian fat pad. J Vis Exp. 2016 Sep 7;(115).

Acknowledgements

This work was supported by NIH grants (CA182413, CA260115 and CA248524) to AYN, Ovarian Cancer Research Fund grant (327516) to AYN, Sandra Atlas Bass Endowment for Cancer Research to AYN and JCS, and the NSF Graduate Research Fellowship Program (GRFP) awarded to CQR (DGE-2139899).

Author contributions

DJP, JCS and AYN designed experiments; DJP, CQR, TME, CSA and APA performed experiments and performed pathological evaluations; AFN and RJY provided resources; DJP wrote the paper; DJP, JCS, AYN revised and edited the paper.

Competing interests: None.

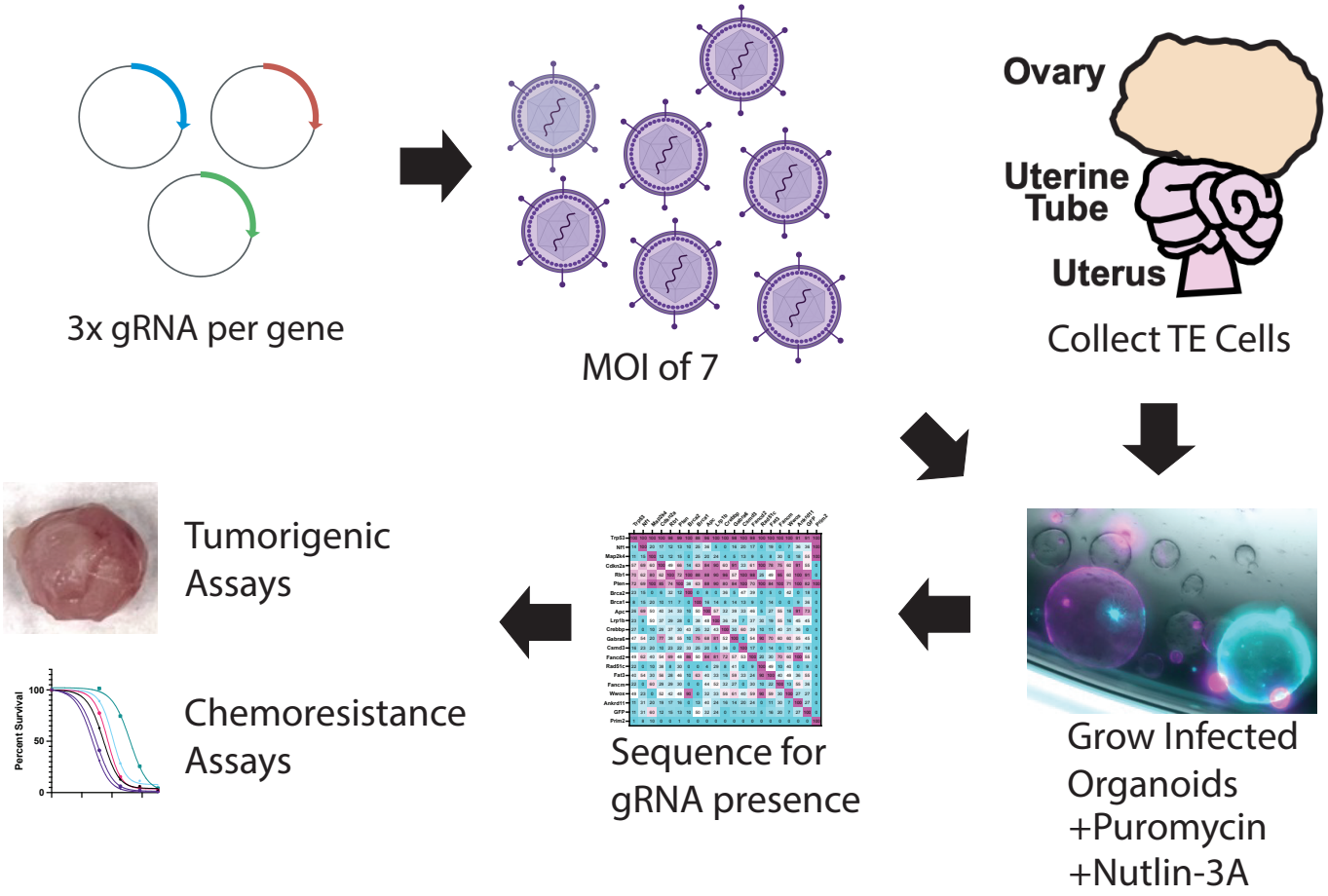

Figure 1. Schematic of screening strategy. Tubal epithelial cells (TE) are from the uterine tube.

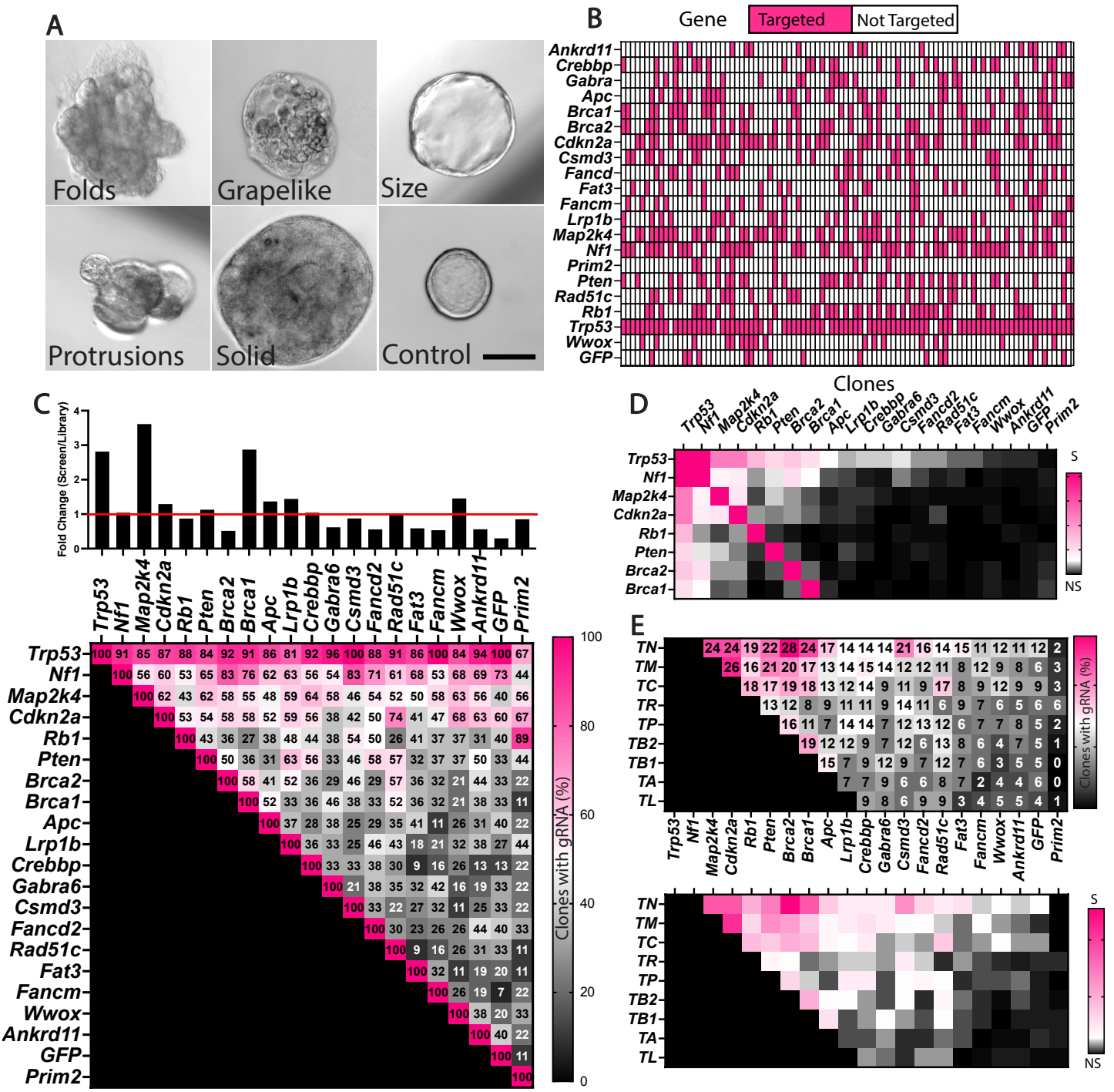

Figure 2. **Mutation combinations in transformed TE organoids**. A) Phenotypes of mutant organoids. Scale bar = 100µm. B) gRNA vectors identified in each aberrant organoid clone. C) Enrichment of targeting vectors in aberrant clones. The fold change was calculated based on % representation in clonal organoids over % representation in library. The red horizontal line represents no representation difference between gRNA frequency found in library and screen. (Bottom) Frequency of co-mutations in organoids. Numbers are percentages. D) $\chi 2$ analysis of significant TE double mutations, DF, 19, P<0.05%, S= Significant, NS= not significant. E) Number of clones that contain gRNA's targeting genes in triple mutations containing the top 9 overrepresented genes in the screen. (Bottom) $\chi 2$ analysis of significant TE triple mutations, DF, 19, P<0.05%. S= Significant, NS= Not Significant.

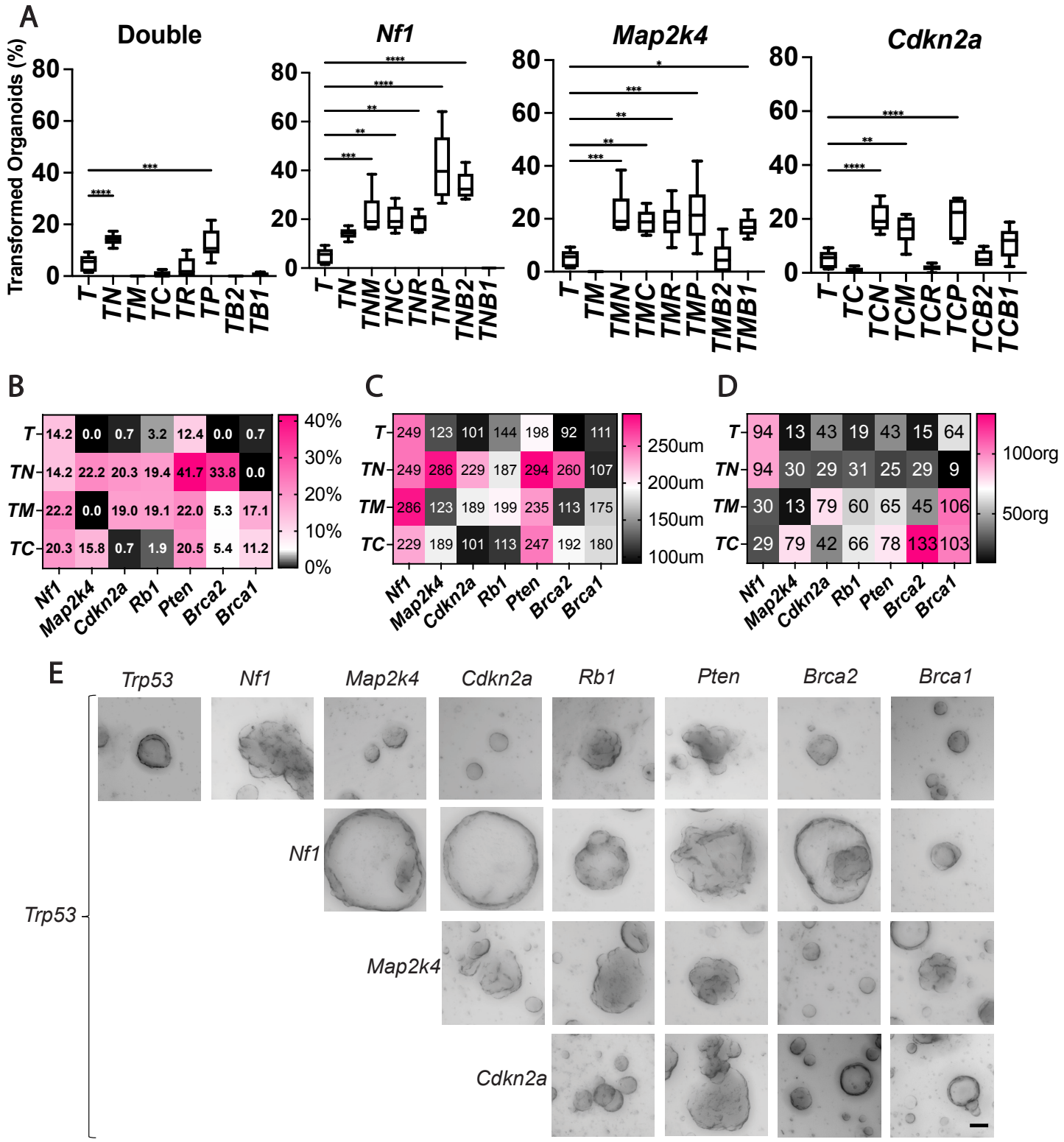

Figure 3. **Validation of mutation combinations driving TE organoid transformation.** Percent transformation of A) Double mutant combinations, Triple mutant combinations with *Nf1*^{mut}, *Map2k4*^{mut} or *Cdkn2a*^{mut} background. B) Organoid transformation percentage of combinations compared to *Trp53*$^{-/-}$ alone. C) Average organoid diameters vs *Trp53*$^{-/-}$ alone D) Average organoid (org) formation vs *Trp53*$^{-/-}$ alone. E) Representative images of organoids for each combination tested. Scale bar = 100µm. One-way anova was used to assess significance, n=6 per condition. P-value < * = 0.05, <** = 0.01, <*** = 0.001, <****= 0.0001.

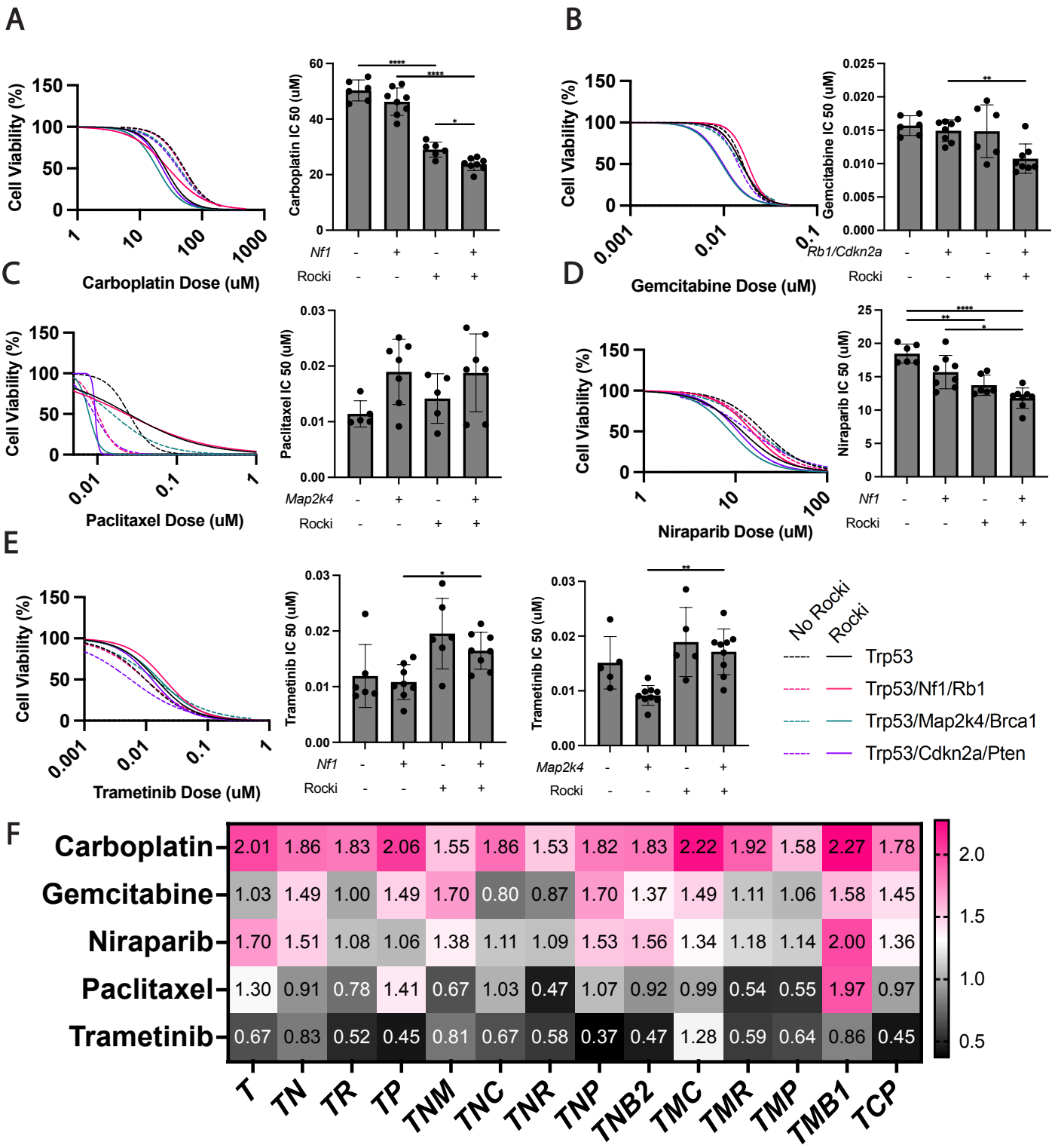

Figure 4. **Impacts of mutations on drug responses.** Dose response curves were performed and combinations representing most of the genes were graphed. A) Carboplatin, *Nf1*^{mut} are 22% more resistant to carboplatin B) Gemcitabine, *Rb1*^{mut}*Cdkn2a*^{mut} are 38% more resistant to gemcitabine C) Paclitaxel, *Map2k4*^{mut} are 25% (with ROCKi) or 40% (without ROCKi) more sensitive to paclitaxel D) Niraparib, *Nf1*^{mut} containing mutants are ~16% more resistant to niraparib. E) Trametinib, *Map2k4*^{mut} are 65% more resistant to trametinib. F) IC50 fold change Rocki- /Rocki+. One-way anova, Brown-Forsythe and Welch Tests were performed to assess differences in sensitivity and resistance. Two independent experiments were conducted per mutation combination in triplicate. One-way anova was used to assess significance. P-value < * = 0.05, <** = 0.01, <*** = 0.001, <****= 0.0001.

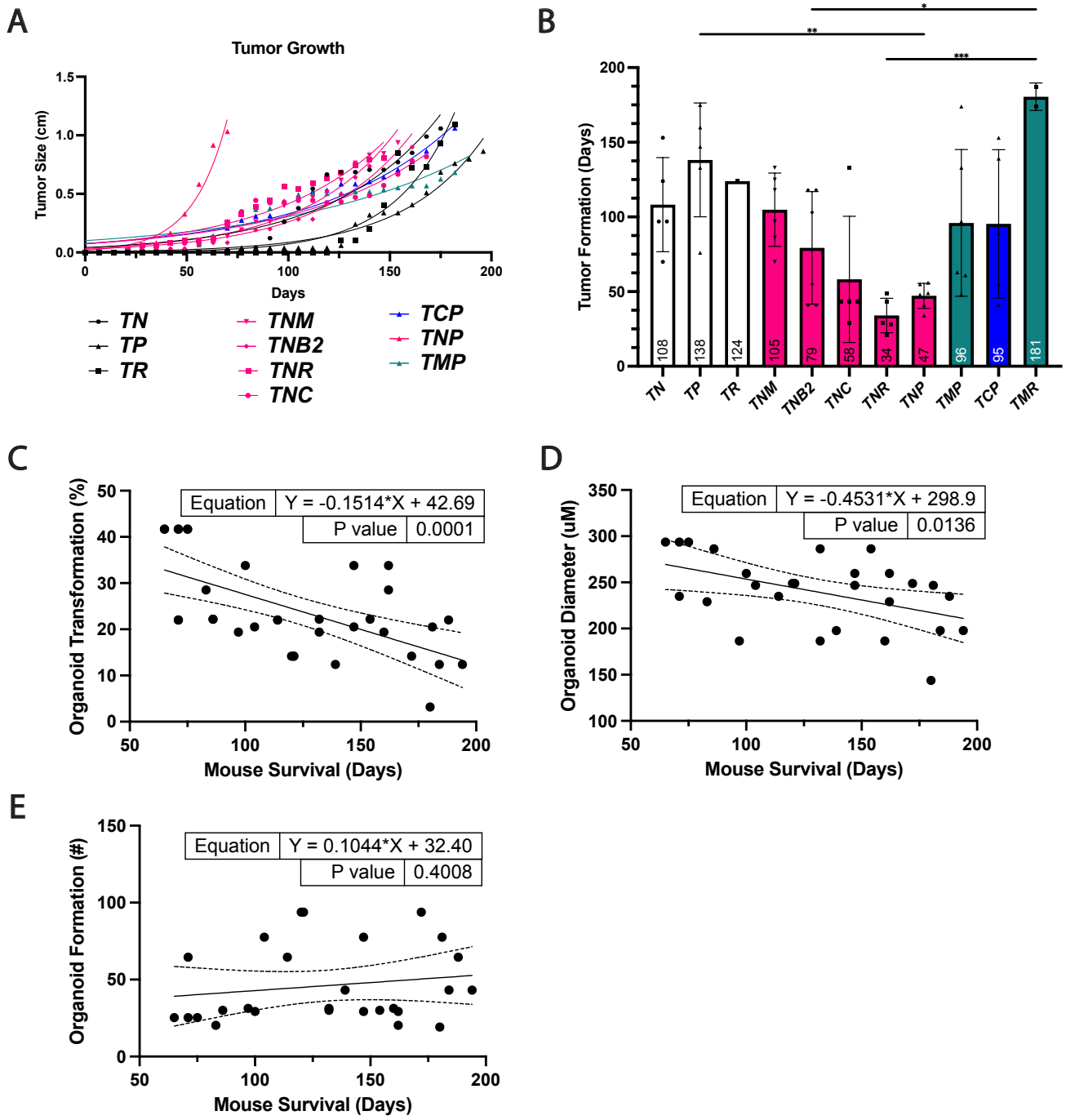

Figure 5. TE organoid transformation reflects tumorigenic potential. A) Tumor growth as measured on a weekly basis. B) Initial tumor formation, when a palpable mass was first observed. One-way anova was used to assess significance. P-value < * = 0.05, <** = 0.01, <*** = 0.001, <****= 0.0001. C-E) Organoid metrics mapped against mouse survivability.

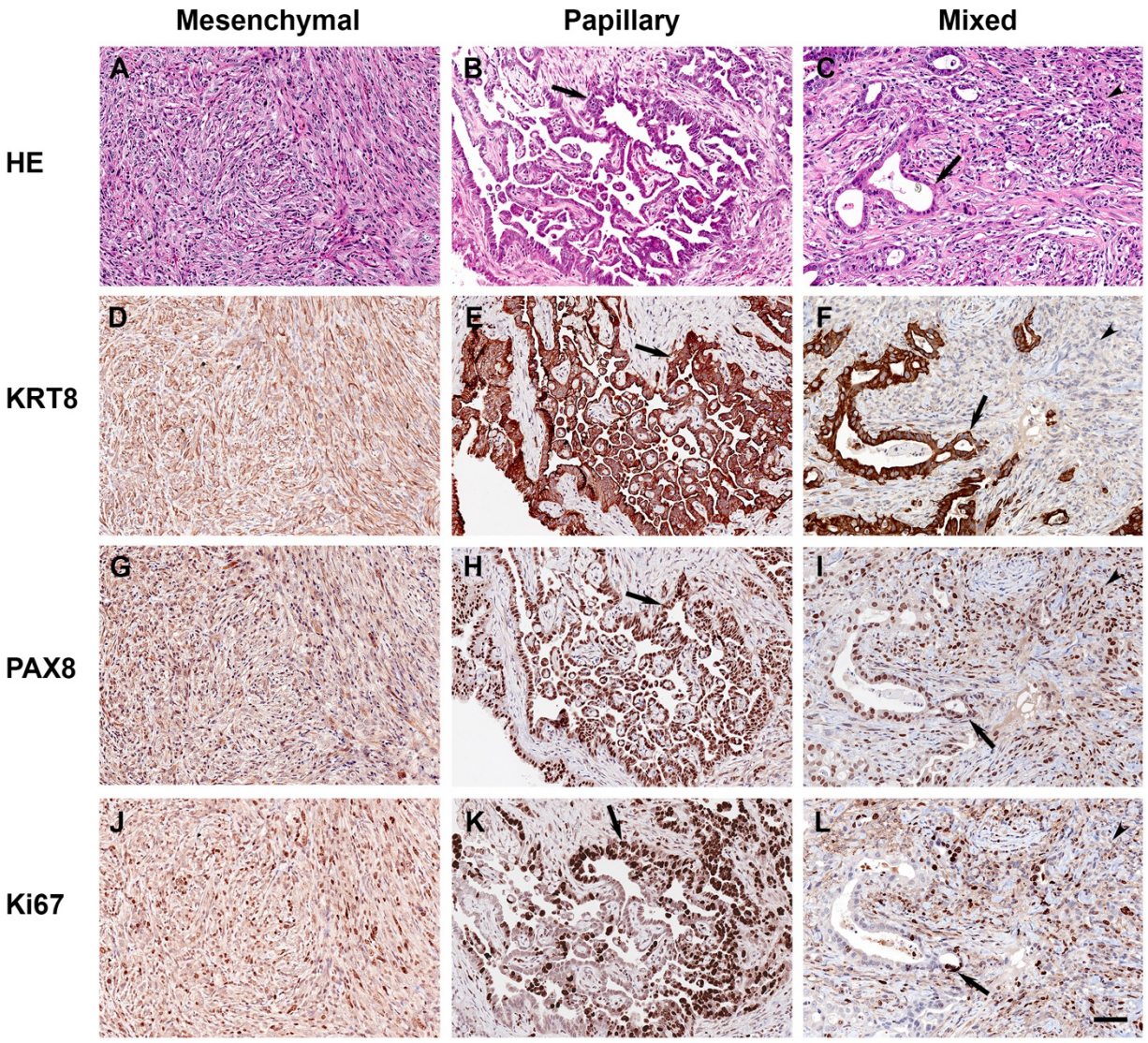

Figure 6. Characterization of neoplasms arising from genetically altered TE organoid cells transplanted subcutaneously. A) Spindle-cell (Mesenchymal) neoplasm with monotonous tight growth pattern, TN. B) Papillary carcinoma (Papillary) with slit-like spaces forming complex labyrinthine pattern (arrow), TP. C) Neoplasm with mixed spindle-cell (arrowhead) and glandular (arrow) patterns of growth (Mixed), TMP. Hematoxylin and eosin (HE; A-C). D-L) Expression (brown color) of KRT8 (D-F), PAX8 (G-I), and Ki67 (J-L) in neoplastic cells. Counterstaining with hematoxylin (D-L). Scale bar, all panels 60 μm.

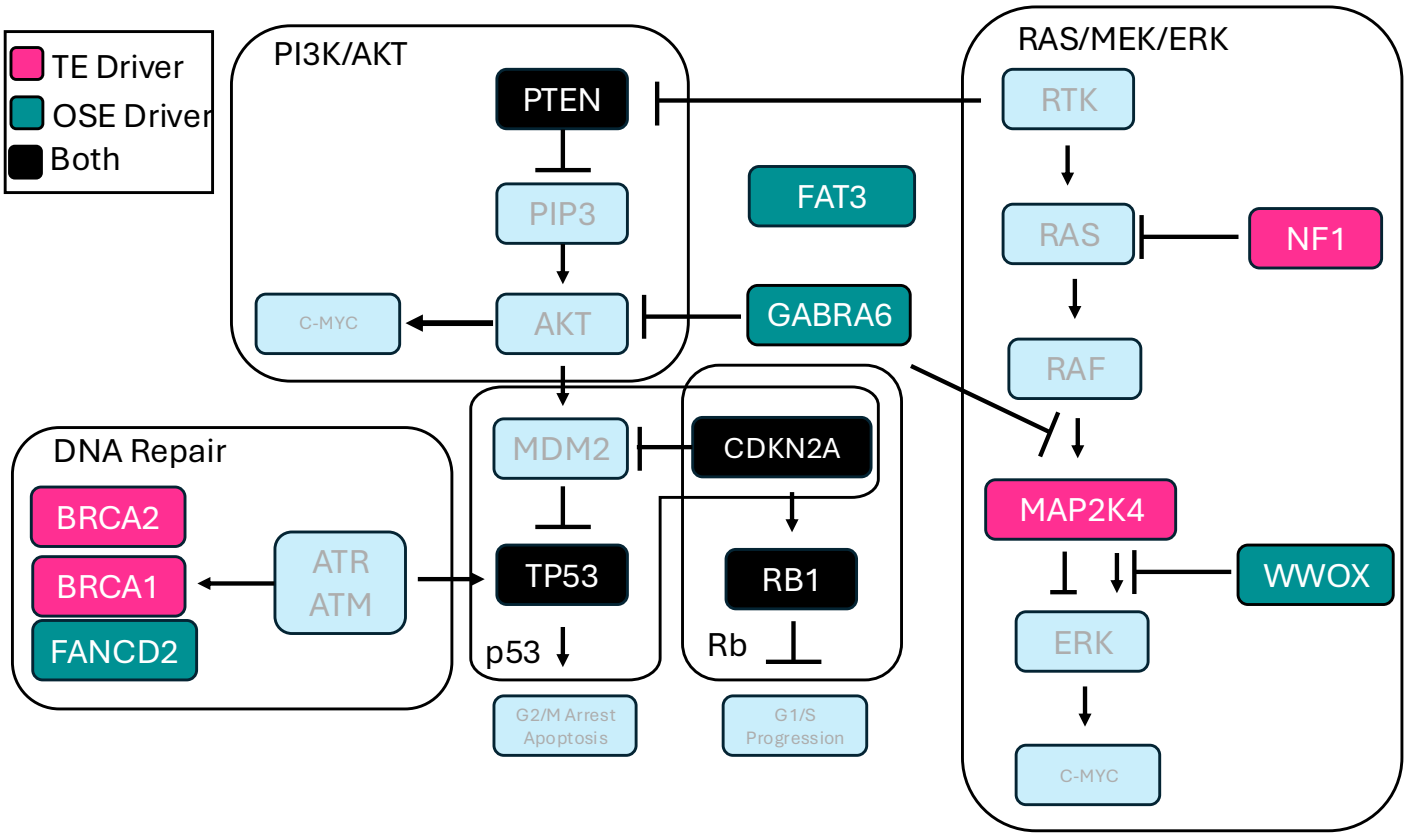

Figure 7. Summary of pathways of gene drivers identified in OSE and TE screens.